Computational Mechanics (2019) 64:1655–1667
https://doi.org/10.1007/s00466-019-01743-x

ORIGINAL PAPER

Crack-face frictional contact modelling in cracked piezoelectric materials

Luis Rodríguez-Tembleque[1] · Felipe García-Sánchez[2] · Andrés Sáez[1]

Received: 17 October 2018 / Accepted: 8 June 2019 / Published online: 24 June 2019

Abstract
Actuators, sensors, micro- and nano-electromechanical systems and other piezoelectirc components are generally constructed in block form or as a thin laminated composites. The study of the integrity of such materials in their various forms and small sizes is still a challenge nowadays. To gain a better understanding of these systems, this work presents a crack surface contact formulation that includes friction and thus makes it possible to study the integrity of these advanced materials under more realistic crack surface multifield operational conditions. The dual boundary element method (BEM) is used for modeling frictional crack surface contact on piezoelectric solids in the presence of electric fields, further taking into account the electrical semipermeable boundary conditions on the crack. The formulation uses contact operators over the augmented Lagrangian to enforce contact constraints on the crack surfaces. The BEM reveals to be a very suitable methodology for these interface interaction problems because it considers only the boundary degrees of freedom, what makes it possible to reduce the number of unknowns and to obtain accurate results with a much lower number of elements than formulations based on the standard finite element method or the eXtended finite element method. The capabilities of this methodology are illustrated by solving some benchmark problems.

Keywords Piezoelectric materials · Crack friction · Fracture mechanics · Contact mechanics · Boundary element method · Semipermeable electrical boundary conditions

1 Introduction

Piezoelectric materials exhibit a multifield coupling which allows for their use as actuators and sensors in many technological sectors of current interest, such as the aerospace and automotive industries, or the biomedical and the electronics industries. Actuators, sensors, micro- and nano-electromechanical systems and other PE components are generally constructed in block form or in a thin laminated composite. The study of the integrity of such materials in their various forms and small sizes is still a challenge nowadays [1–3].

In general, crack surface contact problems is a key aspect that should be considered to study integrity problems [4–6]. These pioneering (analytical) works showed that, when a closed crack is considered in an elastic material, it is necessary to know the contact condition of the crack surface to avoid, for instance, physically unrealistic interpenetration of the crack surfaces or over estimation of stress intensity factors. Moreover, the crack surface roughness also alters the direction of crack propagation [7] so it influences the crack path [8]. Consequently, several numerical methodologies have been developed to provide engineers with computational tools to consider crack surface frictional contact in fractured materials. Due to the extremely good accuracy that the Boundary Element Method (BEM) presents in fracture mechanics problems, several works [9–14] have studied the influence of contact during the last thirty years. This problem have also been tackled considering other numerical techniques like finite element (FE) formulations with enrichment

✉ Luis Rodríguez-Tembleque
luisroteso@us.es

Felipe García-Sánchez
fgsanchez@uma.es

Andrés Sáez
andres@us.es

[1] Escuela Técnica Superior de Ingeniería, Universidad de Sevilla, Camino de los Descubrimientos s/n, 41092 Seville, Spain

[2] Escuela de Ingenierías Industriales, Universidad de Málaga, Doctor Ortiz Ramos s/n, 29071 Málaga, Spain

functions, i.e., extended FE method (XFEM) [15–18], new advanced FE strategies [19] or a scaled boundary finite element methodologies (SBFEM) [2].

However, to the best of the authors' knowledge, numerical framework has never been proposed for modeling crack face frictional contact problem in fractured piezoelectric materials. The BEM has been proven as one of the more suitable numerical formulation to study fracture in piezoelectric materials for the last twenty years [20–25]. The BEM considers only the boundary degrees of freedom involved in this multifield problem and allows us to obtain a very good accuracy with a low number of elements. During those years, some boundary element based formulations proposed how to consider nonlinear electrical and mechanical crack face boundary conditions in fractured piezoelectric (PE) materials [26,27], or in magneto-electro-elastic (MEE) materials [28,29], considering the crack-face electromagnetic boundary conditions for fracture of magnetoelectroelastic materials presented in [30]. Although several authors have modeled the case of normal contact conditions between crack faces [26,31–33], frictional contact conditions were not considered in those works. Moreover, recent works on mulfield materials under contact conditions [34–37] have revealed the strong influence of friction on the contact pressures, stress and electric/magnetic fields.

In this context, this work presents a crack surface contact formulation which makes it possible to study the integrity of these advanced materials under more realistic crack surface multifield operational conditions. The dual BEM [38,39] is used for modeling frictional crack surface contact on piezoelectric solids, in the presence of electric fields and using a singe-domain formulation that permits to easily include the more realistic semipermeable electrical boundary conditions on the crack, while avoiding the need to define multiple domains in order to incorporate the crack geometry [40]. The formulation, based on previous works [23,26,34–36], uses the BEM for computing the elastic influence coefficients and contact operators over the augmented Lagrangian to enforce contact constraints on the crack surface. The capabilities of this methodology are illustrated by solving some benchmark problems.

The remainder of this work is organized as follows. Section 2 presents the problem description. Sections 3 and 4 present the crack face mechanical and electrical contact boundary conditions, respectively. The literature on BEM formulations is quite extensive, so in Sect. 5 we briefly present the basic ideas of a dual boundary element formulation to tackle fracture problems in piezoelectric materials. The discrete crack surface contact nonlinear equations set is presented in Sect. 6 and the solution scheme is summarized in Sect. 7. Section 8 presents the numerical results and discussion and, finally, Sect. 9 concludes the paper.

2 Problem formulation

Let us consider a two-dimensional, homogeneous, anisotropic and linear piezoelectric (PE) cracked solid $\Omega \subset \mathbb{R}^2$ with boundary $\partial\Omega$ (see Fig. 1), in a Cartesian coordinate system (x_i) $(i = 1, 2)$. The mechanical equilibrium equations for this problem, in the absence of body forces, and the electric equilibrium equations under free electrical charge are

$$\begin{aligned} \sigma_{ij,j} &= 0 \quad \text{in} \quad \Omega, \\ D_{i,i} &= 0 \quad \text{in} \quad \Omega, \end{aligned} \tag{1}$$

where σ_{ij} are the components of Cauchy stress tensor and D_i are the electric displacements. The infinitesimal strain tensor γ_{ij} and the electric field E_i are defined as

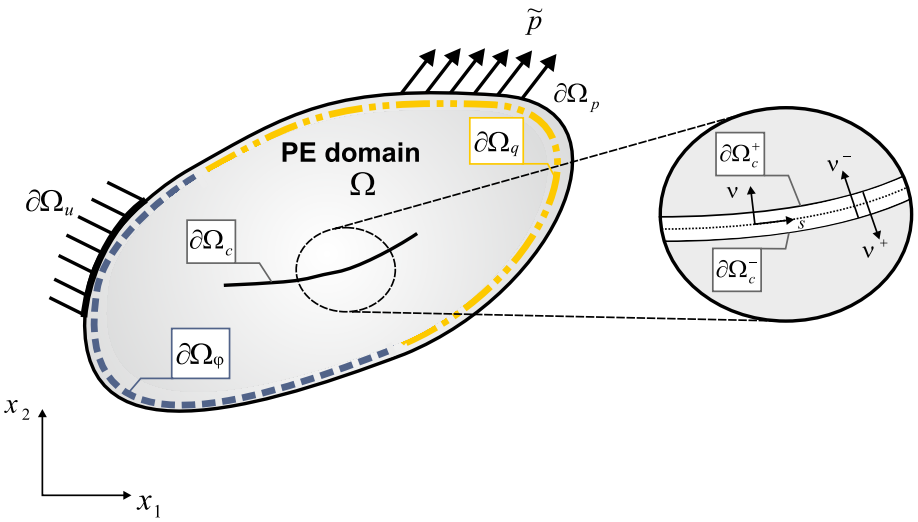

Fig. 1 Fractured piezoelectric domain

$$\begin{array}{ll} \gamma_{ij} = (u_{i,j} + u_{j,i})/2 & \text{in } \Omega, \\ E_i = -\varphi_{,i} & \text{in } \Omega, \end{array} \tag{2}$$

with u_i being the elastic displacement and φ being the electric potential.

The elastic and electric fields are coupled through the linear constitutive law

$$\begin{array}{ll} \sigma_{ij} = c_{ijkl}\gamma_{kl} - e_{lij}E_l & \text{in } \Omega, \\ D_i = e_{ikl}\gamma_{kl} + \epsilon_{il}E_l & \text{in } \Omega, \end{array} \tag{3}$$

where c_{ijkl} and ϵ_{il} denote the components of the elastic stiffness tensor and the dielectric permittivity tensor, respectively; and e_{ijk} are the PE coupling coefficients. These tensors satisfy the following symmetries: $c_{ijkl} = c_{jikl} = c_{ijlk} = c_{klij}$, $e_{kij} = e_{kji}$, $\epsilon_{kl} = \epsilon_{lk}$, with the elastic constant and dielectric permittivity tensors being positive definite.

The boundary $\partial\Omega$ is divided in two disjoint parts: $\partial\Omega = \partial\Omega_e \cup \partial\Omega_c$, where $\partial\Omega_e$ denotes the external boundary and $\partial\Omega_c$ is the crack surface. Two partitions of the boundary $\partial\Omega_e$ are considered to define the mechanical and the electrical boundary conditions. The first partition is: $\partial\Omega_e = \partial\Omega_u \cup \partial\Omega_p$, i.e., $\partial\Omega_u$ being the external boundary on which diplacements $\tilde{u}_i$ are prescribed and $\partial\Omega_p$ with imposed tractions $\tilde{p}_i$. The second partition is: $\partial\Omega_e = \partial\Omega_\varphi \cup \partial\Omega_q$, being the electrical potential $\tilde{\varphi}$ prescribed on $\partial\Omega_\varphi$, and the electrical charges $\tilde{q}$ assumed on $\partial\Omega_q$. Consequently, the Dirichlet boundary conditions are

$$\begin{array}{ll} u_i = \tilde{u}_i & \text{on } \partial\Omega_u, \\ \varphi = \tilde{\varphi} & \text{on } \partial\Omega_\varphi, \end{array} \tag{4}$$

and the Neumann boundary conditions are given by

$$\begin{array}{ll} \sigma_{ij}\nu_j = \tilde{p}_i & \text{on } \partial\Omega_p, \\ D_i\nu_i = \tilde{q} & \text{on } \partial\Omega_q, \end{array} \tag{5}$$

with ν_i being the outward unit normal to the boundary.

Finally, on the upper and lower crack faces (i.e. $\partial\Omega_c = \partial\Omega_c^+ \cup \partial\Omega_c^-$) self equilibrated tractions and electric charges are considered: $\Delta p_i = p_i^+ + p_i^- = 0$ and $\Delta q = q^+ + q^- = 0$. However, aditional crack surface contact conditions have to be considered, as follows, on $\partial\Omega_c$.

3 Crack face mechanical contact conditions

In order to avoid material interpepenetration between crack-faces, the unilateral contact law involves Signorini's contact conditions on $\partial\Omega_c$:

$$\Delta u_\nu \geq 0, \;\; p_\nu^+ \geq 0, \;\; \Delta u_\nu \; p_\nu^+ = 0, \tag{6}$$

where $\Delta u_\nu = u_\nu^+ - u_\nu^-$ and $p_\nu^+ = \mathbf{p}^+ \cdot \boldsymbol{\nu}_c^+$, with $\boldsymbol{\nu}_c^+$ being the unit normal on $\partial\Omega_c^+$.

The normal contact constraints presented in (6) can be formulated as:

$$p_\nu^+ - \mathbb{P}_{\mathbb{R}_+}(\widehat{p}_\nu^+) = 0, \tag{7}$$

where $\mathbb{P}_{\mathbb{R}_+}(\cdot)$ is the normal projection function ($\mathbb{P}_{\mathbb{R}_+}(\cdot) = max(0, \cdot)$) and $\widehat{p}_\nu^+ = p_\nu^+ - r_\nu \Delta u_\nu$ is the augmented normal traction. The parameters r_ν is the normal dimensional penalization parameter ($r_\nu \in \mathbb{R}^+$).

In general, frictional contact condition on crack surfaces should be considered. So the Coulomb friction restriction can be summarized as:

$$\Delta u_\tau = -\lambda p_\tau^+, \;\; \lambda \geq 0, \;\; |p_\tau^+| \leq \mu p_\nu^+, \;\; \lambda(p_\tau^+ - \mu p_\nu^+) = 0, \tag{8}$$

where λ is an scalar, μ is the friction coefficient, $\Delta u_\tau = u_\tau^+ - u_\tau^-$ and $p_\tau^+ = \mathbf{p}^+ \cdot \boldsymbol{\tau}_c^+$, with $\boldsymbol{\tau}_c^+$ being the unit tangential vector on $\partial\Omega_c^+$.

The frictional contact constraints (8) can be also formulated using a contact operators as:

$$p_\tau^+ - \mathbb{P}_{\mathbb{E}_\rho}(\widehat{p}_\tau^+) = 0, \tag{9}$$

where $\widehat{p}_\tau^+ = p_\tau^+ - r_\tau \Delta u_\tau$ is the augmented tangential traction, r_τ being the tangential dimensional penalization parameter ($r_\tau \in \mathbb{R}^+$), and $\mathbb{P}_{\mathbb{E}_\rho}(\cdot) : \mathbb{R} \longrightarrow \mathbb{R}$ is the tangential projection function defined as

$$\mathbb{P}_{\mathbb{E}_\rho}(\widehat{p}_\tau^+) = \begin{cases} \widehat{p}_\tau^+ & \text{if } |\widehat{p}_\tau^+| < \rho, \\ \rho(\widehat{p}_\tau^+/|\widehat{p}_\tau^+|) & \text{if } |\widehat{p}_\tau^+| \geq \rho, \end{cases} \tag{10}$$

with $\rho = \mu p_\nu^+$, as it was defined in Eq. (7).

4 Crack face electrical contact conditions

The electrical boundary conditions on the crack-faces $\partial\Omega_c$ can be defined in the general form as

$$q^+ = \kappa_c \Delta\varphi / \Delta u_\nu, \tag{11}$$

where $\Delta\varphi = \varphi^+ - \varphi^-$. In Eq. (4), κ_c is the electrical permittivity of the medium between the crack faces and it is defined by the product of the relative permittivity of the considered medium (κ_r) and the permittivity of the vacuum ($\kappa_o = 8.85 \times 10^{-3}$ C/(GVm)): $\kappa_c = \kappa_r \kappa_o$. So, in contrast to the impermeable or the permeable crack-face boundary conditions, this expression presents a non-linear relation between mechanical displacements, electrical potential and electrical charges.

In order to consider both semi-permeable crack-face conditions and crack-face contact conditions, Eq. (4) is redefined as $q^+ = \tilde{\kappa}\Delta\varphi/\Delta u_\nu$,

$$\tilde{\kappa} = \begin{cases} \kappa_c & \text{if } \Delta u_\nu > 0, \\ \infty & \text{if } \Delta u_\nu = 0. \end{cases} \tag{12}$$

According to (12), the electrical contact condition shows that when there is no contact (i.e. crack opening displacements $\Delta u_\nu > 0$) on $\partial\Omega_c$, the normal component of the electric displacement field is $q^+ = \kappa_c\Delta\varphi/\Delta u_\nu$, $\partial\Omega_c$ being the permittivity parameter that allows us to impose permeable, impermeable or semipermeable crack face conditions. Nevertheless, when there is contact (i.e., $\Delta u_\nu = 0$, and consequently $\tilde{\kappa} = \infty$), electric potentials on the crack faces are the same: $\Delta\varphi = 0$.

5 Boundary integral equations

The dual formulation for the BE solution of crack problems considers both the extended displacement (EDBIE) and the extended traction (ETBIE) boundary integral representations to overcome the difficulty of having two coincident boundaries $\partial\Omega_c^+$ and $\partial\Omega_c^-$. In this way, the EDBIE is applied for collocation points $\boldsymbol{\xi}$ on $\partial\Omega_e$ and on either of the crack faces, say $\partial\Omega_c^-$, to yield

$$c_{IJ}(\boldsymbol{\xi})u_J(\boldsymbol{\xi}) + \int_{\partial\Omega} p^*_{IJ}(\mathbf{x},\boldsymbol{\xi})u_J(\mathbf{x})dS(\mathbf{x}) = \int_{\partial\Omega} u^*_{IJ}(\mathbf{x},\boldsymbol{\xi})p_J(\mathbf{x})dS(\mathbf{x}), \tag{13}$$

where $\mathbf{x}$ is a boundary point, u_J is the extended displacement vector (see Barnett and Lothe representation [41])

$$u_J = \begin{cases} u_j & J \leqslant 2 \\ \varphi & J = 3, \end{cases} \tag{14}$$

p_J is the extended tractions vector

$$p_J = \begin{cases} p_j & J \leqslant 2 \\ q & J = 3, \end{cases} \tag{15}$$

c_{IJ} depends on the local geometry of the boundary $\partial\Omega$ at the collocation point $\boldsymbol{\xi}$; u^*_{IJ} and p^*_{IJ} are the extended displacement fundamental solution and the extended traction fundamental solution at a boundary point $\mathbf{x}$ due to a unit extended source applied at point $\boldsymbol{\xi}$, respectively [20] .

Consequently, the ETBIE is applied for collocation points $\boldsymbol{\xi}$ on the other crack surface, $\partial\Omega_c^+$,

$$c_{IJ}(\boldsymbol{\xi})p_J(\boldsymbol{\xi}) + \oint_{\partial\Omega} s^*_{IJ}(\mathbf{x},\boldsymbol{\xi})u_J(\mathbf{x})dS(\mathbf{x}) = \int_{\partial\Omega} d^*_{IJ}(\mathbf{x},\boldsymbol{\xi})p_J(\mathbf{x})dS(\mathbf{x}), \tag{16}$$

to complete the set of equations to compute the extended displacements and tractions on $\partial\Omega$. In Eq. (16) s^*_{IJ} and d^*_{IJ} are obtained by differentiation of u^*_{IJ} and p^*_{IJ} [20], as

$$d^*_{IJ}(\mathbf{x},\boldsymbol{\xi}) = -N_s(\boldsymbol{\xi})C_{sIKr}u^*_{KJ,r}(\mathbf{x},\boldsymbol{\xi}), \tag{17}$$

$$s^*_{IJ}(\mathbf{x},\boldsymbol{\xi}) = -N_s(\boldsymbol{\xi})C_{sIKr}p^*_{KJ,r}(\mathbf{x},\boldsymbol{\xi}), \tag{18}$$

with $N_s(\boldsymbol{\xi})$ being the outward unit normal to the boundary at the source point and

$$C_{iJKl} = \begin{cases} C_{ijkl}, & J,K = 1,2 \\ e_{lij}, & J = 1,2;\ K = 3 \\ e_{ikl}, & J = 3;\ K = 1,2 \\ -\epsilon_{il}, & J,K = 3, \end{cases} \tag{19}$$

where the lowercase (elastic) and uppercase (extended) subscripts take values 1, 2 and 1, 2, 3, respectively. Furthermore, Symbols $\oint$ and $\oiint$ in Eqs. (13) and (16) stand for the Cauchy Principal Value (CPV) and the Hadamard Finite Part (HFP) of the integral, respectively.

When the cracks are mechanically and electrically self-equilibrated, i.e., $\Delta p_I = p_I^+ + p_I^- = 0$ on $\partial\Omega_c$ (the superscripts $+$ and $-$ stand for the upper and lower crack surfaces), it would be enough to apply the EDBIE for collocation points $\boldsymbol{\xi}$ on $\partial\Omega_e$ and the ETBIE for collocation points $\boldsymbol{\xi}$ on either side of the crack, say $\partial\Omega_c^+$, to yield

$$c_{IJ}(\boldsymbol{\xi})u_J(\boldsymbol{\xi}) + \int_{\partial\Omega_e} p^*_{IJ}(\mathbf{x},\boldsymbol{\xi})u_J(\mathbf{x})dS(\mathbf{x}) + \int_{\partial\Omega_c^+} p^*_{IJ}(\mathbf{x},\boldsymbol{\xi})\Delta u_J(\mathbf{x})dS(\mathbf{x}) = \int_{\partial\Omega_e} u^*_{IJ}(\mathbf{x},\boldsymbol{\xi})p_J(\mathbf{x})dS(\mathbf{x}) \tag{20}$$

$$p_I(\boldsymbol{\xi}) + \oint_{\partial\Omega_e} s^*_{IJ}(\mathbf{x},\boldsymbol{\xi})u_J(\mathbf{x})dS(\mathbf{x}) + \oiint_{\partial\Omega_c^+} s^*_{IJ}(\mathbf{x},\boldsymbol{\xi})\Delta u_J(\mathbf{x})dS(\mathbf{x}) = \oint_{\partial\Omega_e} d^*_{IJ}(\mathbf{x},\boldsymbol{\xi})p_J(\mathbf{x})dS(\mathbf{x}) \tag{21}$$

Equations (20) and (21) yield a complete set of equations to compute the extended displacements and tractions on $\partial\Omega_e$ and the extended crack opening displacements $\Delta u_I = u_I^+ - u_I^-$ on $\partial\Omega_c$. In Eq. (21), as previously discussed in Ref. [23], the free term c_{IJ} has been set to 1 because of the additional singularity arising from the coincidence of the two crack surfaces.

6 Crack surface contact discrete equations

Numerical evaluation of the ETBIE requires C^1 continuity of the displacements. As in previous works [23], discontin-

uous quadratic elements with the two extreme collocation nodes shifted towards the element interior are used to mesh the cracks. The asymptotic behavior of the extended displacements near the crack tip is modelled via discontinuous quarter-point elements. For the rest of the boundaries, continuous quadratic elements are employed. A detailed justification of the discretization procedure can be found in [23].

A collocation procedure on boundary integral equations (20) and (21) leads to the following system of equations: $\mathbf{A}\mathbf{x} = \mathbf{F}$, where the boundary conditions have been imposed and all the unknowns have been passed to vector $\mathbf{x}$, to yield

$$\left[\mathbf{A}_{\mathrm{x}_e}\ \mathbf{A}_{\Delta u_c}\ \mathbf{A}_{\Delta\varphi_c}\ \mathbf{A}_{p_c}\ \mathbf{A}_{q_c}\right]\left\{\begin{array}{c}\mathbf{x}_e\\ \Delta\mathbf{u}_c\\ \Delta\boldsymbol{\varphi}_c\\ \mathbf{p}_c\\ \mathbf{q}_c\end{array}\right\} = \mathbf{F}. \tag{22}$$

In expression (22), $\mathbf{x}_e$ collects the nodal external unknowns (i.e. the nodal unknowns on $\partial\Omega_e$), $\Delta\mathbf{u}_c$ and $\Delta\boldsymbol{\varphi}_c$ collect the nodal crack opening displacements and electric potentials, respectively, on $\mathbf{x}_c$, $\mathbf{p}_c$ contains the normal and tangential nodal contact tractions (i.e. $\mathbf{p}_\nu$ and $\mathbf{p}_\tau$) and $\mathbf{q}_c$ contains the nodal electric charges. Matrices $\mathbf{A}_{\mathrm{x}_e}$, $\mathbf{A}_{\Delta u_c}$, $\mathbf{A}_{\Delta\varphi_c}$, $\mathbf{A}_{p_c}$ and $\mathbf{A}_{q_c}$ are constructed with the columns of matrices yielded from the numerical integration of Eqs. (20) and (21).

The electric charge on every contact node i can be expressed in terms of the electric potential according to the electrical contact condition (4), as: $(\mathbf{q}_c)_i = -\tilde{\kappa}((\Delta\mathbf{u}_\nu)_i)(\Delta\boldsymbol{\varphi}_c)_i$. So equation (22) can be written as

$$\left[\mathbf{A}_{\mathrm{x}_e}\ \mathbf{A}_{\Delta u_c}\ \tilde{\mathbf{A}}_{\Delta\varphi_c}\ \mathbf{A}_{p_c}\right]\left\{\begin{array}{c}\mathbf{x}_e\\ \Delta\mathbf{u}_c\\ \Delta\boldsymbol{\varphi}_c\\ \mathbf{p}_c\end{array}\right\} = \mathbf{F}, \tag{23}$$

being $\tilde{\mathbf{A}}_{\Delta\varphi_c} = \mathbf{A}_{\Delta\varphi_c} - \tilde{\boldsymbol{\kappa}}(\Delta\mathbf{u}_\nu)\mathbf{A}_{q_c}$ and $\tilde{\boldsymbol{\kappa}}(\Delta\mathbf{u}_\nu)$ a diagonal matrix, i.e.:

$$\tilde{\boldsymbol{\kappa}}(\Delta\mathbf{u}_\nu) = diag\left(\tilde{\kappa}((\Delta\mathbf{u}_\nu)_1), \ldots, \tilde{\kappa}((\Delta\mathbf{u}_\nu)_i), \ldots, \tilde{\kappa}((\Delta\mathbf{u}_\nu)_{N_c})\right). \tag{24}$$

Finally, the mechanical contact restrictions (7) and (9) are defined on every contact node i as:

$$(\mathbf{p}_\nu)_i - \mathbb{P}_{\mathbb{R}_+}\left((\mathbf{p}_\nu)_i - r_\nu(\Delta\mathbf{u}_\nu)_i\right) = 0, \tag{25}$$

$$(\mathbf{p}_\tau)_i - \mathbb{P}_{\mathbb{E}_\rho}\left((\mathbf{p}_\tau)_i - r_\tau(\Delta\mathbf{u}_\tau)_i\right) = 0, \tag{26}$$

where $\mathbf{p}_\nu$ and $\mathbf{p}_\tau$ contain the normal and tangential contact tractions of every contact node i and $\Delta\mathbf{u}_\nu$ and $\Delta\mathbf{u}_\tau$ contain the normal and tangential nodal crack opening displacements, respectively.

7 Solution method

The nonlinear equations set (23–26) can be solved using different solution schemes according to [42,43]. In this work, the system (23–26) will be solved using the Uzawa's method. This iterative solution scheme is presented in [42,44–46] and more recently in [47–49], for contact and wear problems, and in [34,36], for multifield PE materials in contact.

To compute the variables on load step (k), $\mathbf{z}^{(k)} = (\mathbf{x}_e^{(k)}, \Delta\mathbf{u}_c^{(k)}, \Delta\boldsymbol{\varphi}_c^{(k)}, \mathbf{p}_c^{(k)})$, when the variables on previous instant $\mathbf{z}^{(k-1)}$ are known:

(I) Initialize $\mathbf{z}^{(0)} = \mathbf{z}^{(k-1)}$ and iterate using (n) index.

(II) Solve:

$$\left[\mathbf{A}_{\mathrm{x}_e}\ \mathbf{A}_{u_c}\ (\mathbf{A}_{\varphi_c} - \tilde{\boldsymbol{\kappa}}(\mathbf{p}_\nu^{(n)})\mathbf{A}_{q_c})\right]\left\{\begin{array}{c}\mathbf{x}_e\\ \Delta\mathbf{u}_c\\ \Delta\boldsymbol{\varphi}_c\end{array}\right\}^{(n+1)} = -\mathbf{A}_{p_c}\,\mathbf{p}_c^{(n)} + \widetilde{\mathbf{F}}, \tag{27}$$

where $\widetilde{\mathbf{F}} = \mathbf{F} - (\tilde{\boldsymbol{\kappa}}^{(n)}/\Delta\boldsymbol{\Phi}^{(n)})\mathbf{A}_{q_c}$, $\tilde{\boldsymbol{\kappa}}^{(n)}$ is a diagonal matrix that depends on the contact status of every contact node and $\Delta\boldsymbol{\Phi}^{(n)}$ is a diagonal matrix defined as: $\Delta\boldsymbol{\Phi}^{(n)} = diag((\Delta\boldsymbol{\varphi}_c^{(n)})_1, \ldots, (\Delta\boldsymbol{\varphi}_c^{(n)})_i, \ldots, (\Delta\boldsymbol{\varphi}_c^{(n)})_{N_c})$.

(III) Update contact tractions and contact status for every contact node i:

$$(\mathbf{p}_\nu^{(n+1)})_i = \mathbb{P}_{\mathbb{R}_-}\left((\mathbf{p}_\nu^{(n)})_i + r_\nu(\Delta\mathbf{u}_\nu^{(n+1)})_i\right), \tag{28}$$

$$(\mathbf{p}_\tau^{(n+1)})_i = \mathbb{P}_{\mathbb{E}_\rho}\left((\mathbf{p}_\tau^{(n)})_i - r_\tau\,(\Delta\mathbf{u}_\tau^{(n+1)})_i\right), \tag{29}$$

where $\rho = \mu|(\mathbf{p}_\nu^{(n+1)})_i|$. So if $(\mathbf{p}_\nu^{(n+1)})_i < 0$, node i is assumed to be in contact.

(IV) Update diagonal matrix $\tilde{\boldsymbol{\kappa}}^{(n+1)}$ as a function of the contact status computed in previous step.

(V) Compute the error $\Psi(\mathbf{z}^{(n+1)}) = max\{\|\Delta\mathbf{u}_c^{(n+1)} - \Delta\mathbf{u}_c^{(n)}\|, \|\Delta\boldsymbol{\varphi}_c^{(n+1)} - \Delta\boldsymbol{\varphi}_c^{(n)}\|, \|\mathbf{p}_c^{(n+1)} - \mathbf{p}_c^{(n)}\|\}$.

(a) If $\Psi(\mathbf{z}^{(n+1)}) \leq \varepsilon$, the solution for the instant (k) is reached, so $\mathbf{z}^{(k)} = \mathbf{z}^{(n+1)}$.

(b) Otherwise, return to (II) evaluating: $\mathbf{p}_c^{(n)} = \mathbf{p}_c^{(n+1)}$ and $\boldsymbol{\kappa}^{(n)} = \boldsymbol{\kappa}^{(n+1)}$.

After the solution at step (k) is reached, the solution for the next step is achieved by setting: $\mathbf{z}^{(0)} = \mathbf{z}^{(k)}$ and returning to (I).

8 Numerical examples

The previously sketched formulation offers a suitable framework to study the influence of crack face frictional con-

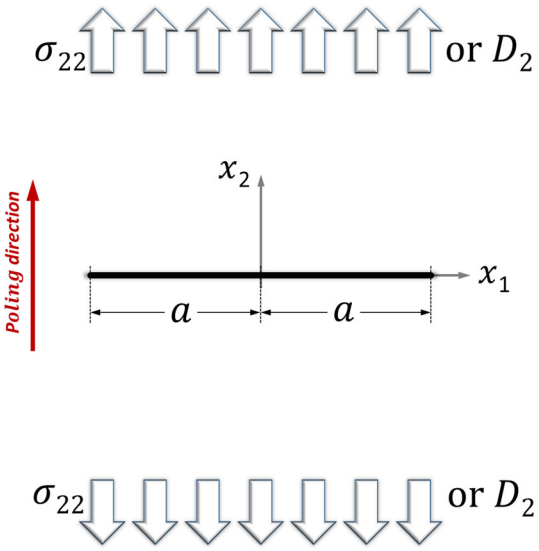

Fig. 2 Crack in an infinite domain under far field uniform stress (σ_{22}) and electric displacements (D_2)

Table 1 Material properties of PZT-4, from [20]

Elastic coefficients (GPa)	
C_{11}	139.00
C_{12}	74.30
C_{22}	115.00
C_{66}	25.60
Piezoelectric coefficients (C/m^2)	
e_{21}	− 5.2
e_{22}	15.1
e_{16}	12.7
Dielectric constants (C/(GV m))	
ϵ_{11}	6.461
ϵ_{22}	5.62

tact and nonlinear electric boundary conditions on fracture response of piezoelectric materials. In order to validate the formulation and to understand the influences of these factors, several benchmark problems have been studied.

8.1 Crack in unbounded domain

The first example corresponds to a finite straight crack along the x_1-direction in an infinite PZT-4 plane under a uniform far field stress or electric displacement (see Fig. 2). This example allows us to check the formulation under nonlinear electrical crack face boundary conditions. The material constants are shown in Table 1, the axis of symmetry of the material being the x_2-axis. Moreover, to mesh the crack, five quadratic elements are considered, crack tip elements being discontinuous quarter-point elements.

The obtained crack opening displacements in normal direction and electric potential increment along the crack due to an uniform electric displacements loading: $D_2 = 1C/m^2$ are shown in Fig. 3a, b, respectively. Results in Fig. 3 are presented in a non-dimensional form, $\Delta u_{v,o}$ and $\Delta\varphi_o$ being the crack opening displacements and the electric potential increment, respectively, obtained in [30] for impermeable crack-face electric boundary conditions . It can observed how the permittivity parameter κ_c clearly affects the crack opening displacements and the electric potential increment along the crack. Moreover, the results are compared with the known exact analytical solution obtained by [30] for ideal crack-face electric boundary conditions (i.e., impermeable and permeable conditions), showing an excellent agreement. The extended crack opening displacement components Δu_I for the ideal crack-face electric boundary conditions can be written as

$$\Delta u_I = 2\mathbf{Y}_{IJ}\left(\sigma_{J2}^{\infty} - \sigma_{J2}^{c}\right)\sqrt{a^2 - x_1^2}, \tag{30}$$

where σ_{J2}^{∞} are the applied extended stresses, σ_{J2}^{c} are the extended stresses on the crack surfaces and $\mathbf{Y}$ is the compliance (Irwin) matrix, as defined in [23]. In the expression above, the repeated indexes implies summation.

Same conclusions were observed in Fig. 4 for an uniform traction loading: $\sigma_{22} = 1\,\text{GPa}$, where it may be observed a perfect agreement between the numerical and the analytical solutions for impermeable and permeable crack-face electric boundary conditions. The increase of Δu_v caused by the increase of the κ_c value in Fig. 4a is due to the fact that both the mechanical and the electrical fields are fully coupled, as it may be observed in the compliance (Irwin) matrix.

To illustrate the convergence of the proposed solution scheme under nonlinear crack-face electrical boundary conditions, convergence studies have been included for the case of a Griffith crack in a piezoelectric material. Figure 5 shows the relative error evolution $(\Psi(\mathbf{z}^{(n)})/\Psi(\mathbf{z}^{(o)}))$ with the number of iterations for several meshes and different values of the permittivity parameter (κ_c). Results reveal that the proposed methodology is robust and accurate. While the number of iterations is hardly affected by the number of elements used to mesh the crack, it is however significantly affected by the severity of the nonlinear crack-face electrical boundary conditions: a low number of iterations have been observed for fully permeable or fully impermeable electrical conditions, whereas a greater number of iterations are required for convergence when semipermeable conditions hold on the crack-faces.

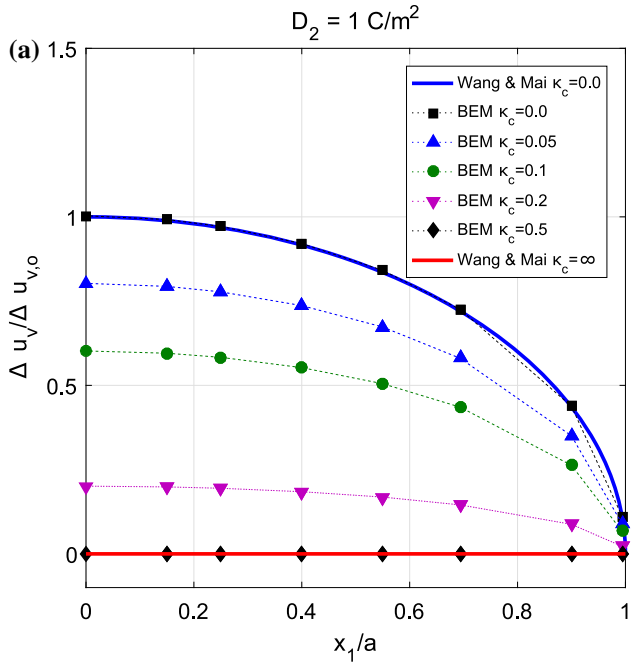

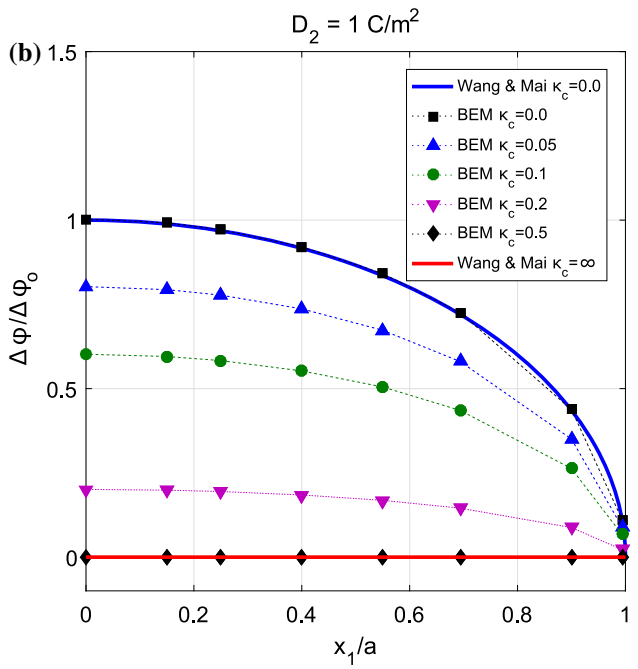

Fig. 3 Influence of the permittivity parameter κ_c on: **a** the crack opening displacements and **b** the electric potential increment along the crack due to an uniform electric displacements loading: $D_2 = 1\,\mathrm{C/m^2}$

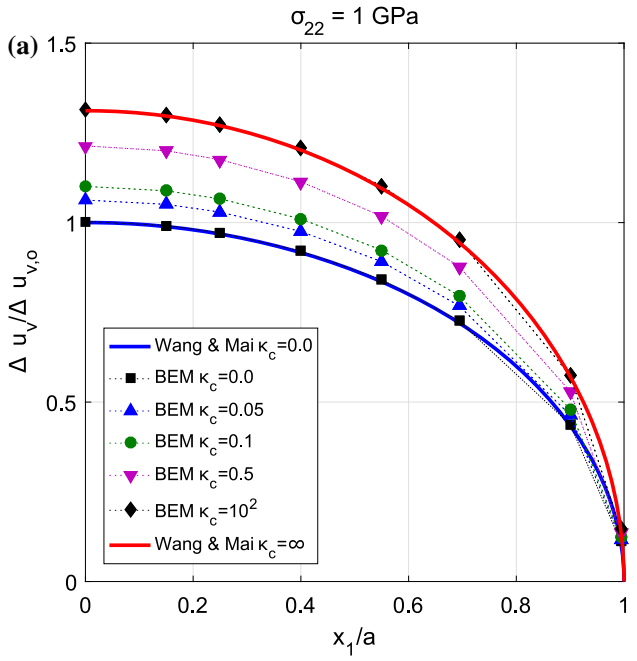

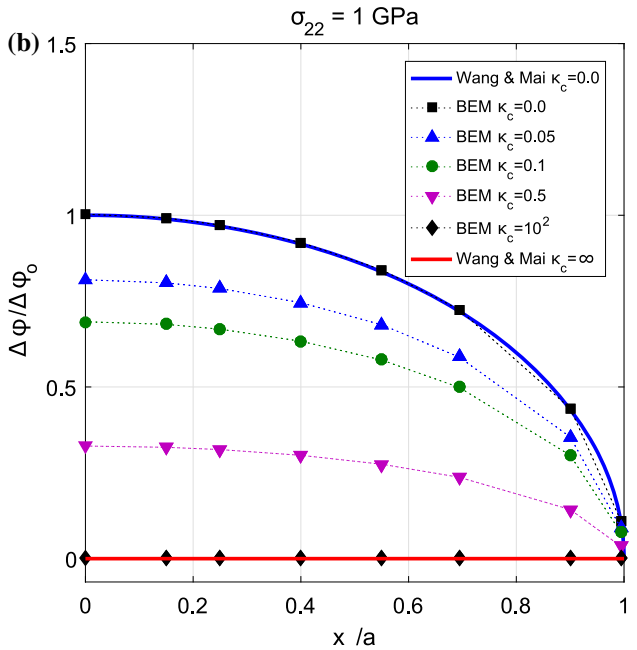

Fig. 4 Influence of the permittivity parameter κ_c on: **a** the crack opening displacements and **b** the electric potential increment along the crack for uniform traction loading: $\sigma_{22} = 1\,\mathrm{GPa}$

The influence of the permittivity parameter κ_c on extended stress intensity factors: K_I, K_{II} and K_{IV}, for the uniform electric displacements loading is presented in Fig. 6. According to [23,50], those extended stress intensity factors are determined from the nodal values from the extended crack opening displacements across the crack, as

$$\begin{pmatrix} K_{II} \\ K_I \\ K_{IV} \end{pmatrix} = \sqrt{\frac{\pi}{8\bar{r}}}\mathbf{Y}^{-1} \begin{pmatrix} \Delta u_1 \\ \Delta u_2 \\ \Delta\varphi \end{pmatrix}, \tag{31}$$

where, in this case, the $\bar{r}$ is the distance between the crack tip and the extreme node of the quarter-point elements and K_{IV} denotes the electric displacement intensity factor.

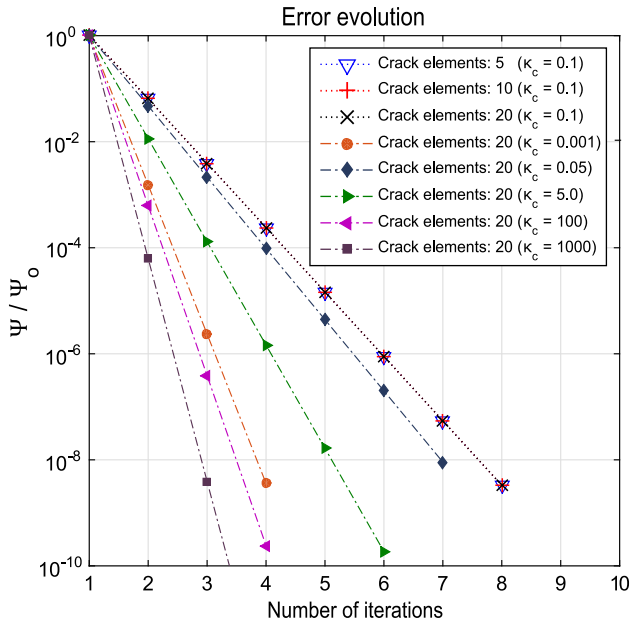

Fig. 5 Error evolution for several meshes and different values of the permittivity parameter (κ_c)

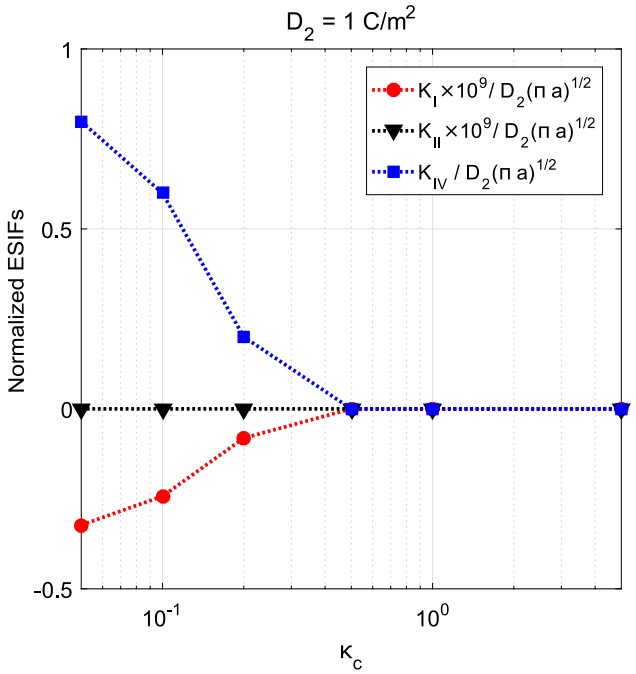

Fig. 6 Influence of the permittivity parameter κ_c on the intensity factors K_I, K_{II} and K_{IV} for the uniform electric displacements loading $D_2 = 1\,\mathrm{C/m^2}$

Finally, results in Fig. 6 correspond to the crack subjected to an uniform remote electric displacements loading and depicts the intensity factors. Consequently, when the permittivity parameter κ_c increases, i.e., when perfect permeable crack-face boundary conditions are considered, the extended stress intensity factors tend to zero.

8.2 Inclined crack under compression

In order to validate this crack surface frictional contact formulation, another benchmark problem is solved. In this example, the formulation is applied for a mathematical degenerate case, i.e., elastic and isotropic material. Figure 7 shows a single crack of length $2a$ in an unbounded domain and subjected to a compressive remote stress σ (i.e., $\sigma_{11} = -\sigma$). The analytical solution of this plane strain state is available in [4] for comparison. The mode-I stress intensity factor (SIF) $K_I = 0$, as the crack surfaces remain closed under compression. However, the analytical solution for the mode-II SIF is

$$K_{II} = \sigma\sqrt{\pi a}\,\sin\alpha(\cos\alpha - \mu\sin\alpha) \tag{32}$$

where μ can be written as a function of the friction angle (ϕ): $\mu = tan(\phi)$.

The material constants employed are: Young's modulus $E = 70\ GPa$ and Poisson's ratio $\nu = 0.2$. Results are presented in Fig. 8, where the normalized K_{II} ($K_{II}/\sigma\sqrt{\pi a}$) is showed for various inclination angles (α) of the crack and different friction angles ($\phi = 0°, 15°, 30°, 45°$). An excellent agreement between analytical and numerical solutions can be observed. In this example, nonlinear crack-face mechanical boundary conditions (i.e. frictional contact) are considered for electroelastic problems. The convergence ratios observed for the Uzawa scheme in these examples are analogous to the ratios observed in [49] for frictional contact problems using the BEM in elastic problems.

After validating the frictional contact methodology, this formulation is now applied for a piezoelectric material whose properties are presented in Table 1. In order to study only the influence of frictional contact conditions on cracked piezoelectric materials, Sects. 8.2 and 8.3 show two benchmark problems presented in the literature, where impermeable crack face boundary conditions (i.e., $\kappa_c = 0$) are considered. Figure 9 shows the normalized stress (K_I, K_{II}) and electric (K_{IV}) intensity factors at the tip of the crack due to remote tension for different crack orientation angles (α) and differ-

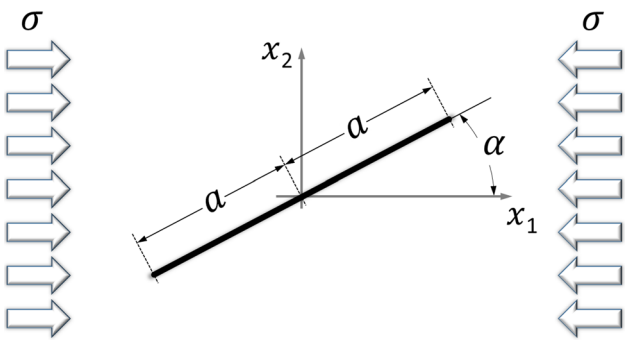

Fig. 7 A crack under compression in an unbounded domain

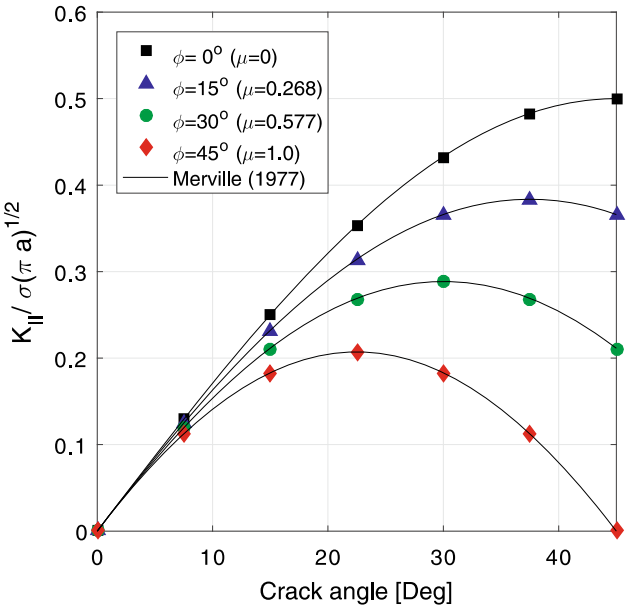

Fig. 8 Numerical results vs. analytical solutions for normalized K_{II} ($K_{II}/\sigma\sqrt{\pi a}$) for various inclination angles (α) and different friction angles (ϕ)

ent friction angles (ϕ). The extended stress intensity factors (ESIF), i.e., K_I, K_{II} and K_{IV}, were computed according to (31). Due to the mechanical and electrical fully coupled compliance (Irwing) matrix, the crack-face tangential slip (Δu_τ) causes not null ESIFs values. The ESIFs in Fig. 9 show the same behavior that has been observed in Fig. 7: when the crack angle (α) is equal or greater than the friction angle (ϕ), i.e., $\alpha \geq \phi$, the crack-face is subject to stick conditions. So the values of the ESIFs become null. Results show again the enormous influence of friction on the stress and electric intensity factors and, consequently, on the integrity of these systems. Therefore, modeling friction is mandatory in order to obtain valid results.

8.3 Branched crack

This example considers a branched crack in an unbounded plane, whose geometry is shown in Fig. 10. The material is PZT-4 and the material constants are given in Table 2. The axis of symmetry of the material is the x_2-axis and the main crack is along the x_1-axis with a branch with an angle θ initiating from one of the crack tips. Five quadratic elements are considered to mesh the main crack. Two equal length elements are used for the branch when its length is $b = a/10$ and nine elements when $b = a/2$. Crack tip elements are discontinuous quarter-point. The crack is under a uniform far field stress along the y-axis and the ESIF are evaluated in accordance to Eq. (31).

Crack branching is a common phenomenon in the fracture of brittle materials. However, the multifield coupling makes

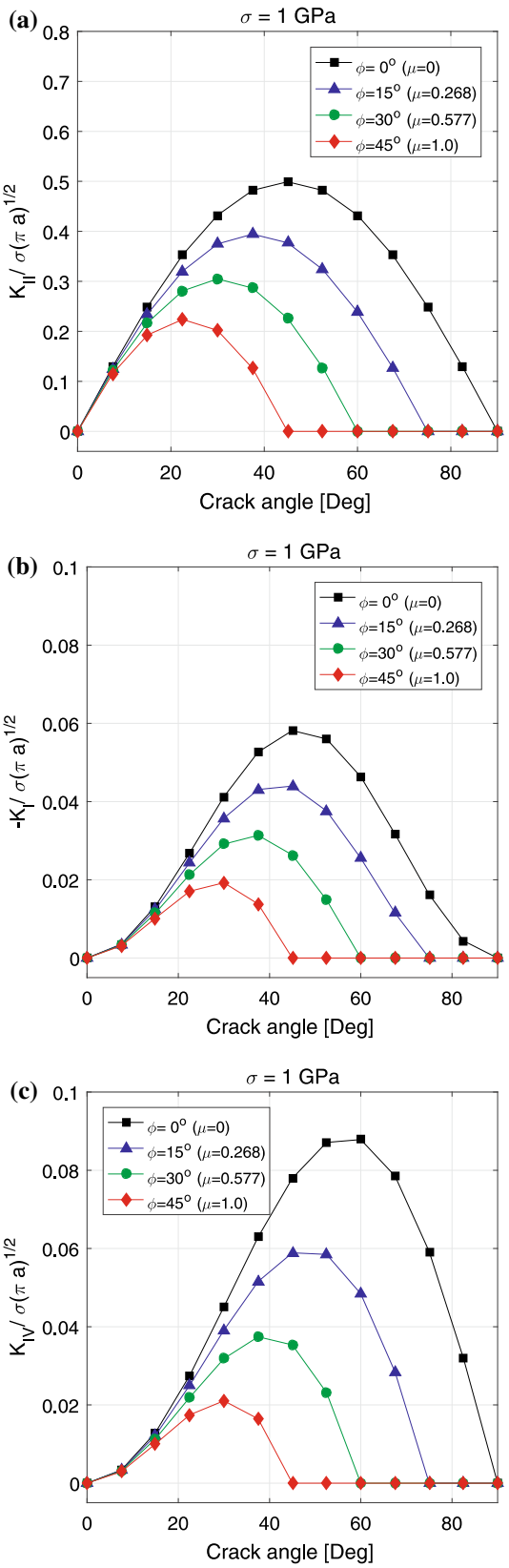

Fig. 9 Normalized stress (K_I, K_{II}) and electric (K_{IV}) intensity factors at the tip of the crack due to remote tension for different crack orientation angles (α) and different friction angles (ϕ)

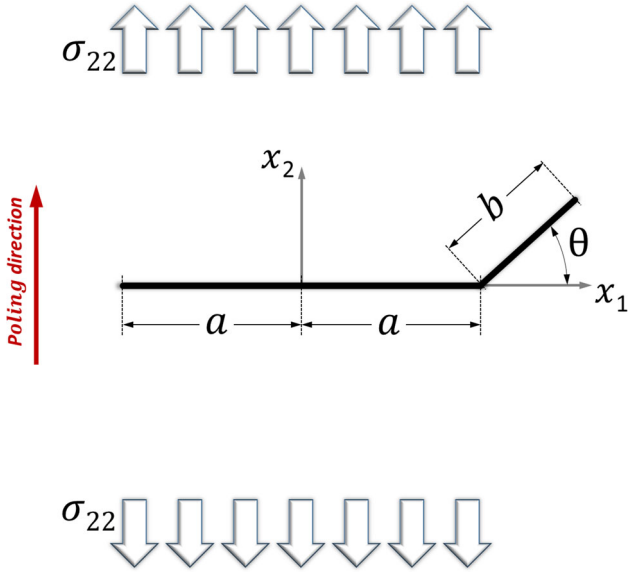

Fig. 10 A branched crack under uniform traction in an unbounded domain

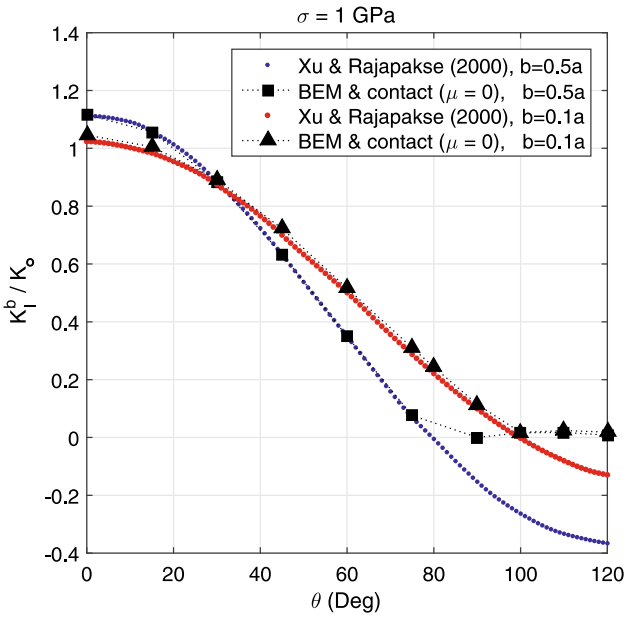

Fig. 11 Normalized stress intensity factors K_I at the tip of a branched crack due to remote tension: K_I^b/K_o, being $K_o = \sigma\sqrt{\pi a}$. Comparison between the boundary element solution including frictionless ($\mu = 0$) contact and the analytical solution from [21] for different branched crack orientation angles (θ) and branch lengths (b)

Table 2 Material properties of PZT-4, from [21]

Elastic coefficients (GPa)	
C_{11}	139.00
C_{12}	74.30
C_{22}	113.00
C_{66}	25.60
Piezoelectric coefficients (C/m^2)	
e_{21}	− 6.98
e_{22}	13.84
e_{16}	13.44
Dielectric constants (C/(GV m))	
ϵ_{11}	6.0
ϵ_{22}	5.47

crack branching more complex for piezoelectric materials than for elastic materials. One of the pioneering works that studied this problem was published by Xu and Rajapakse [21]. They presented a theoretical framework which made it possible to study crack branching on piezoelectric materials. For instance, they presented the values of the ESIF versus the branch angle θ for different lengths of the branch when an uniform traction along the x_2-axis was applied. However, in those cases, no frictional contact conditions were considered on the crack faces. So, crack faces interpenetration were observed for some values of θ and consequently, over- or-under estimated values of the ESIFs were computed.

Figure 11 shows the normalized stress intensity factors K_I at the tip of a branched crack due to remote tension. A comparison between the boundary element solution including frictionless contact and the analytical solution from [21] for different branched crack orientation angles (θ) and branch lengths (b) is considered. We can observe negative values of K_I on [21] when θ is greater than certain value (i.e., $\theta > 90°$ for $b = a/10$ and $\theta > 80°$ for $b = a/2$). Nevertheless, K_I tends to zero for those branch angles when contact is considered. So crack closure is observed when $\theta > 100°$ for $b = a/10$ and $\theta > 90°$ for $b = a/2$.

Next, the influence of frictional contact on the ESIFs is studied in detail for a branch length $b = a/2$. Figure 12 presents the normalized stress (K_I, K_{II}) and electric (K_{IV}) intensity factors at the tip of a branched crack due to remote tension for different branch orientation angles and different friction angles ($\phi = 0°, 15°, 30°, 45°$). Figure 12a shows the normalized stress intensity factor K_I at the tip of a branched crack. As we would expect, friction does not affect K_I, only θ and the normal contact constraints. However, K_{II} and K_{IV} are clearly affected not only by the normal contact constraints, but also by friction. Figure 12b shows how the normalized stress intensity factors K_{II} is affected by crack closure on the branch when $\theta > 90°$. Moreover, significant reduction on K_{II} can be observed as the friction coefficient increases when compared to [21]. Same situation is presented on Fig. 12c for the electric intensity factors K_{IV}. However, in this case, the effect of contact is significantly stronger, i.e., a non-smooth peak on K_{IV} is observed for the crack branching closure around $\theta \approx 90°$. This is due to the combined effect of crack closure (i.e. crack-face contact) and the impermeable electrical crack-face boundary conditions (i.e. $\kappa_c = 0$).

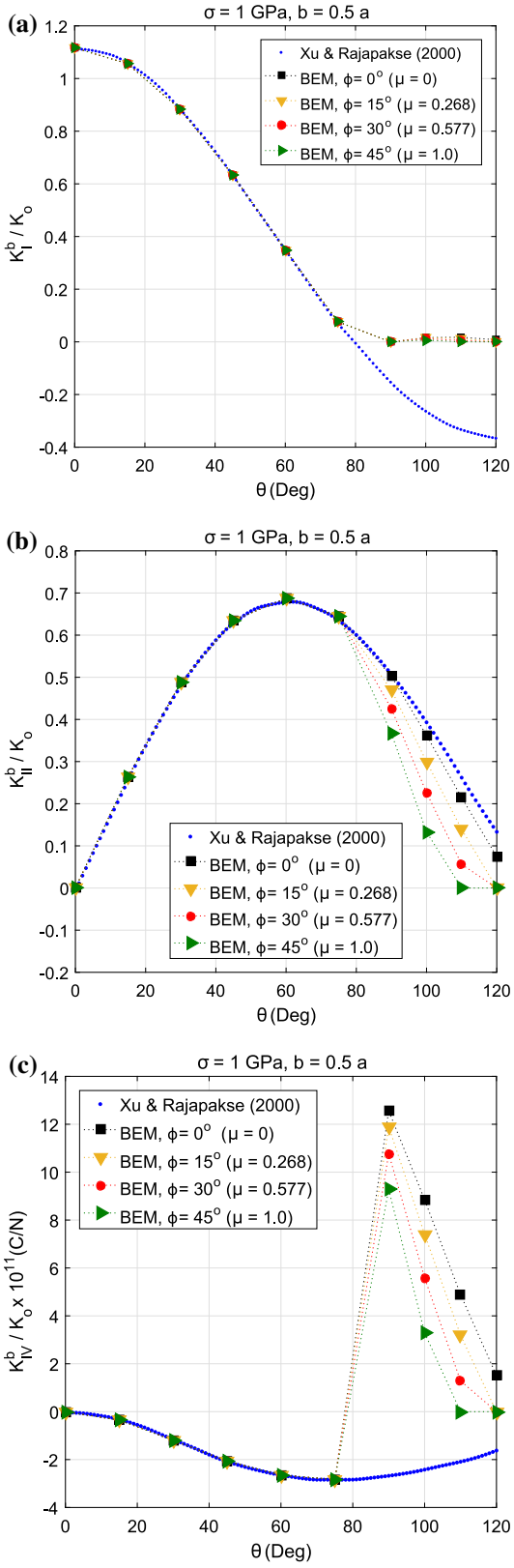

Fig. 12 Influence of frictional contact on the normalized stress (K_I, K_{II}) and electric (K_{IV}) intensity factors at the tip of a branched crack due to remote tension for different branched crack orientation angles (θ), i.e. K_I^b/K_o, K_{II}^b/K_o and K_{IV}^b/K_o, being $K_o = \sigma\sqrt{\pi a}$

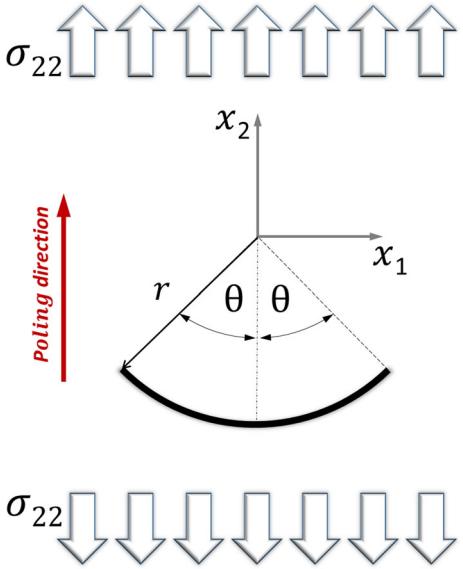

Fig. 13 Curved crack in unbounded domain

Once again, the influence of friction and the need to incorporate this phenomenon in the model is clear from Fig. 12b, c.

8.4 Curved crack in unbounded domain

Finally, to show the use of the current procedure for curved crack geometries, this section presents a curved crack in an unbounded domain (see Fig. 13), where crack-face frictional contact conditions are considered. The crack region is under a uniform far field stress ($\sigma_{22} = 1$ GPa) along the material and crack axis of symmetry. The material properties are the same as in the previous example and they were presented in Table 2. Several cracks for elastic stress loading are analyzed, with semi-angles θ between 0 and 120 degrees.

The computed values of the normalized ESIFs K_I, K_{II} and K_{IV} are shown versus θ in Fig. 14. Similarly to [23], the ratio χ between the dielectric constant ϵ_{22} and the piezoelectric constant e_{22} has been used to represent a dimensionless value of K_{IV}. Computed values of K_I and K_{II} are shown in Fig. 14a, b, respectively, whereas the obtained values of K_{IV} are shown in Fig. 14c. These results show the great influence that crack curvature has on the ESIFs. It may be observed that large values of θ ($\theta \geq 90°$) imply crack closure. Moreover, Fig. 14b shows a significant reduction on K_{II} when the friction coefficient increases. As we mentioned in the previous example, the electric intensity factor K_{IV} presents a non-smooth peak due to the crack closure around $\theta \approx 90°$.

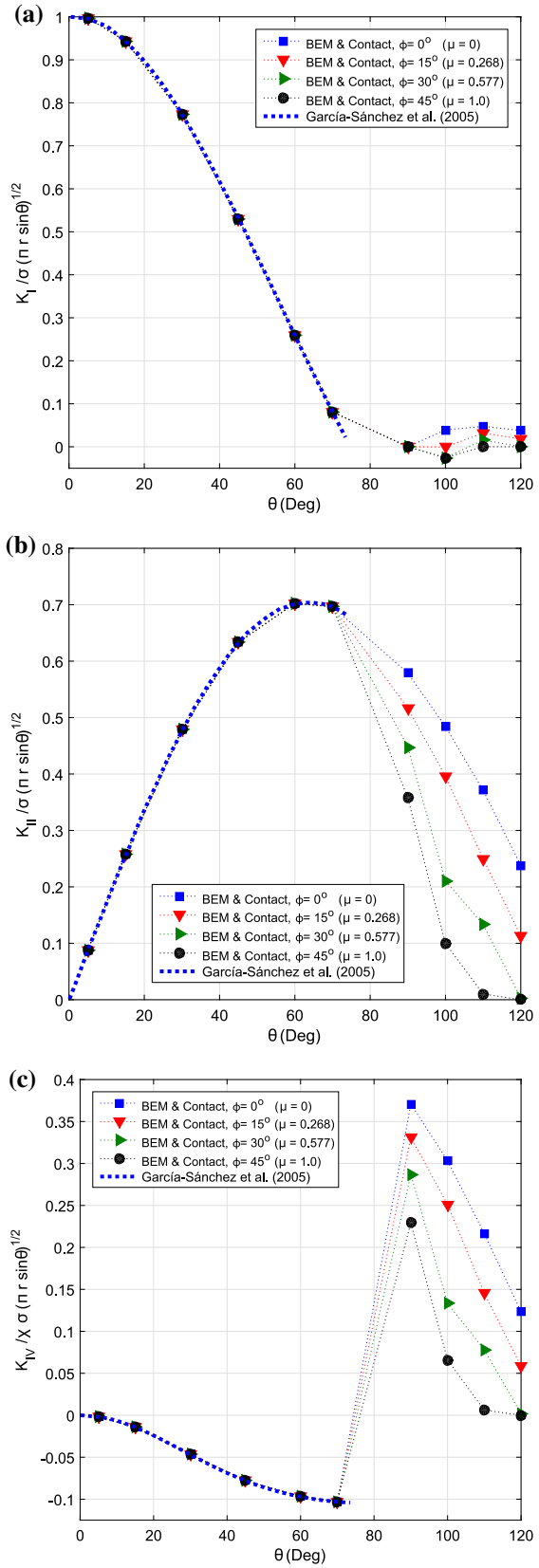

Fig. 14 Influence of frictional contact on the normalized stress (K_I, K_{II}) and electric (K_{IV}) intensity factors at the tip of a curved crack due to remote tension for different curved crack angles (θ)

9 Conclusions

A dual boundary element formulation has been presented and further applied to study fracture phenomena in PE materials. The formulation avoids unrealistic assumptions usually considered for the boundary conditions on the crack surfaces. In particular, it accounts for both surface frictional contact between crack faces and electrically semipermeable boundary conditions. The accuracy and validity of the proposed formulation have been verified by comparison of the obtained numerical results against some classical benchmark problems, exhibiting an excellent agreement with the analytical solution available in the literature. The numerical examples presented reveal the key importance of including friction in the model in order to accurately compute the stress and electric intensity factors in situations where crack closure occurs. Finally, we would like to emphasize that, although the paper contains only examples for crack problems in infinite domains, the boundary element formulation is also valid for bounded domains.

Acknowledgements This work was supported by the *Ministerio de Ciencia e Innovación*, Spain, through the research projects: DPI2014-53947-R and DPI2017-89162-R, which were co-funded by the European Regional Development Fund (ERDF).

References

1. Kuna M (2010) Fracture mechanics of piezoelectric materials where are we right now? Eng Fract Mech 77:309–326
2. Zhang P, Du C, Tian X, Jiang S (2018) A scaled boundary finite element method for modelling crack face contact problems. Comput Methods Appl Eng 328:431–451
3. Lei J, Zhang C (2018) A simplified evaluation of the mechanical energy release rate of kinked cracks in piezoelectric materials using the boundary element method. Eng Fract Mech 188:36–57
4. Merville PH (1977) Fracture mechanics of brittle materials in compression. Int J Fract 13:532–534
5. Comninou M, Dundurs J (1979) On the frictional contact in crack analysis. Eng Fract Mech 12:117–123
6. Cordes RD, Joseph PE (1994) Crack surface contact of surface and internal cracks in a plate with residual stresses. Int J Fract 66:1–17
7. Ballarini R, Plesha ME (1987) The effects of crack surface friction and roughness on crack tip stress fields. Int J Fract 34:195–207
8. Weber W, Willner K, Kuhn G (2010) Numerical analysis of the influence of crack surface roughness on the crack path. Eng Fract Mech 77:1708–1720
9. Zang WL, Gudmundson P (1991) Frictional contact problems of kinked cracks modelled by a boundary integral method. Int J Numer Methods Eng 31:427–446
10. Liu SB, Tan CL (1992) Two-dimensional boundary element contact mechanics analysis of angled crack problems. Eng Fract Mech 42:273–288
11. Chen T-C, Chen W-H (1998) Frictional contact analysis of multiple cracks by incremental displacement and resultant traction boundary integral equations. Eng Anal Bound Elem 21:339–348
12. Phan A-V, Napier JAL, Gray LJ, Kaplan T (2003) Symmetric-Galerkin BEM simulation of fracture with frictional contact. Int J Numer Methods Eng 57:835–851

13. Phan A-V, Napier JAL, Gray LJ, Kaplan T (2003) Stress intensity factor analysis of friction sliding at discontinuity interfaces and junctions. Comput Mech 32:392–400
14. Weber W, Kolk K, Willner K, Kuhn G (2011) On the solution of the 3D crack surface contact problem using the boundary element method. Key Eng Mater 454:11–29
15. Dolbow J, Möes N, Belytschko T (2001) An extended finite element method for modeling crack growth with frictional contact. Comput Methods Appl Eng 190:6825–6846
16. Liu F, Borja RI (2008) A contact algorithm for frictional crack propagation with the extended finite element method. Int J Numer Methods Eng 76:1489–1512
17. Mueller-Hoeppe DS, Wriggers P, Loehnert S (2012) Crack face contact for a hexahedral-based XFEM formulation. Comput Mech 49:725–734
18. Nanthakumar SS, Lahmer T, Zhuang X, Zi G, Rabczuk T (2016) Detection of material interfaces using a regularized level set method in piezoelectric structures. Inverse Probl Sci Eng 24:153–176
19. Nejati M, Paluszny A, Zimmerman R (2018) A finite element framework for modeling internal frictional contact in three-dimensional fractured media using unstructured tetrahedral meshes. Comput Methods Appl Eng 306:123–150
20. Pan E (1999) A BEM analysis of fracture mechanics in 2D anisotropic piezoelectric solids. Eng Anal Bound Elem 23:67–76
21. Xu XL, Rajapakse RKND (2000) A theoretical study of branched cracks in piezoelectrics. Acta Mater 48:1865–1882
22. Rajapakse RKND, Xu XL (2001) Boundary element modeling of cracks in piezoelectrics solids. Eng Anal Bound Elem 25:771–781
23. García-Sánchez F, Sáez A, Domínguez J (2005) Anisotropic and piezoelectric materials fracture analysis by BEM. Comput Struct 83:804–820
24. Groh U, Kuna M (2005) Efficient boundary element analysis of cracks in 2D piezoelectric structures. Int J Solids Struct 42:2399–2416
25. Muñoz-Reja MM, Buroni FC, Sáez A, García-Sánchez F (2016) 3D explicit-BEM fracture analysis for materials with anisotropic multifield coupling. Appl Math Model 40:2897–2912
26. Wünsche M, Zhang C, García-Sánchez F, Sáez A, Sladek J, Sladek V (2011) Dynamic crack analysis in piezoelectric solids with nonlinear electrical and mechanical boundary conditions by a time-domain BEM. Comput Methods Appl Mech Eng 200:2848–2858
27. Wünsche M, Sladek J, Sladek V, Zhang C, García-Sánchez F, Sáez A (2011) Dynamic crack analysis in piezoelectric solids under time-harmonic loadings with a symmetric Galerkin boundary element method. Comput Methods Appl Mech Eng 84:141–153
28. García-Sánchez F, Rojas-Díaz R, Sáez A, Zhang C (2007) Fracture of magnetoelectroelastic matrials using boundary element method (BEM). Theor Appl Fract Mech 47:192–204
29. Rojas-Díaz R, Denda M, García-Sánchez F, Sáez A (2007) Dual BEM analysis of different crack face boundary conditions in 2D magnetoelectroelastic solids. Eur J Mech A Solid 47:192–204
30. Wang B-L, Mai Y-W (2007) Applicability of the crack-face electromagnetic boundary conditions for fracture of magnetoelectroelastic materials. Int J Solids Struct 44:387–398
31. Loboda V, Sheveleva A, Lapusta Y (2014) An electrically conducting interface crack with a contact zone in a piezoelectric bimaterial. Int J Solids Struct 51:63–73
32. Sheveleva A, Lapusta Y, Loboda V (2015) Opening and contact zones of an interface crack in a piezoelectric bimaterial under combined compressive-shear loading. Mech Res Commun 63:6–12
33. Govorukha V, Kamlah M, Loboda V, Lapusta Y (2016) Interface cracks in piezoelectric materials. Smart Mater Struct 25:023001
34. Rodríguez-Tembleque L, Buroni FC, Sáez A (2015) 3D BEM for orthotropic frictional contact of piezoelectric bodies. Comput Mech 56:491–502
35. Rodríguez-Tembleque L, Buroni FC, Sáez A, Aliabadi MH (2016) 3D coupled multifield magneto-electro-elastic contact modelling. Int J Mech Sci 107:36–53
36. Rodríguez-Tembleque L, Sáez A, Aliabadi MH (2016) Indentation response of piezoelectric films under frictional contact. Int J Eng Sci 107:36–53
37. Zhang X, Wang Z, Shen H, Wang QJ (2018) An efficient model for the frictional contact between two multiferroic bodies. Int J Solids Struct 130–131:133–152
38. Hong HK, Chen JT (1988) Derivations of integral equations of elasticity. ASCE J Eng Mech 114:1028–1044
39. Portela A, Aliabadi MH, Rooke DP (1992) The dual boundary element method: effective implementation for crack problems. Int J Numer Methods Eng 33:1269–1287
40. Alaimo A, Milazzo A, Orlando C, Messineo A (2013) Numerical analysis of piezoelectric active repair in the presence of frictional contact conditions. Sensors 13:4390–4403
41. Barnett DM, Lothe J (1975) Dislocations and line charges in anisotropic piezoelectric insulators. Phys Stat Sol (b) 67:105–111
42. Alart P, Curnier A (1991) A mixed formulation for frictional contact problems prone to Newton like solution methods. Comput Methods Appl Mech Eng 92:353–375
43. Christensen PW, Klarbring A, Pang JS, Strömberg N (1998) Formulation and comparison of algorithms for frictional contact problems. Int J Numer Methods Eng 42:145–173
44. Kikuchi N, Oden JT (1988) Contact Problems in Elasticity: A Study of Variational Inequalities and Finite Element Methods. SIAM, Philadelphia
45. Laursen TA (2002) Computational Contact and Impact Mechanics. Springer, Berlin, Heidelberg
46. Wriggers P (2002) Computational Contact Mechanics. Wiley, Chichester
47. Joli P, Feng Z-Q (2008) Uzawa and Newton algorithms to solve frictional contact problems within the bi-potential framework. Int J Numer Methods Eng 73:317–330
48. Rodríguez-Tembleque L, Abascal R, Aliabadi MH (2012) Anisotropic wear framework for 3D contact and rolling problems. Comput Methods Appl Mech Eng 241:1–19
49. Rodríguez-Tembleque L, Abascal R (2013) Fast FE-BEM algorithms for orthotropic frictional contact. Int J Numer Methods Eng 94:687–707
50. Saez A, Gallego R, Dominguez J (1995) Hypersingular quarter-point boundary elements for crack problems. Int J Numer Methods Eng 38:1681–1701